Applied Catalysis B: Environmental 168-169 (2015) 429–440

Contents lists available at ScienceDirect

Applied Catalysis B: Environmental

journal homepage: www.elsevier.com/locate/apcatb

Kinetic modelling of the NO_x reduction by H_2 on $Pt/WO_3/ZrO_2$ catalyst in excess of O_2

Christoph Hahn[a], Matthias Endisch[a], Florian J.P. Schott[b], Sven Kureti[a,*]

[a] Technical University of Freiberg, Institute of Energy Process Engineering and Chemical Engineering, Chair of Reaction Engineering, Fuchsmühlenweg 9, D-09596, Freiberg, Germany
[b] Karlsruhe Institute of Technology, Institute of Technical Chemistry and Polymer Chemistry, D-76128 Karlsruhe, Germany

ARTICLE INFO

Article history:
Received 9 October 2014
Received in revised form
18 December 2014
Accepted 21 December 2014
Available online 27 December 2014

Keywords:
NO_x reduction by H_2
Pt catalyst
Kinetic modelling
Thermodynamic consistency

ABSTRACT

This paper addresses the elementary kinetic mean field modelling of the NO_x reduction by H_2 on $Pt/WO_3/ZrO_2$ under oxygen-rich conditions. $Pt/WO_3/ZrO_2$ was recently shown to reveal substantial low-temperature deNO_x activity with enhanced N_2 selectivity referred to traditional Pt catalysts. The model was developed based on a postulated reaction mechanism as well as kinetic examinations and implied a network of 48 reaction steps described by Arrhenius-based rate expressions. Kinetic parameters were taken from literature and by fitting calculations, while pre-exponential factors of adsorption were estimated from kinetic gas theory. For validation, experiments were simulated and thermodynamic consistency was proven by checking the Gibbs free enthalpy of the catalytic surface reactions. As a result of the kinetic model, the formation of OH surface species was identified as the rate determining step of H_2 oxidation, while the reduction of NO predominately occurs by dissociation of chemisorbed NO.

1. Introduction

Anthropogenic pollutants such as carbon monoxide (CO), hydrocarbons (HC) and nitrogen oxides (NO_x) can cause persistent changes in the biosphere and are increasingly noticed with concern. Thus, an immense number of laws and regulations was remitted for the protection of the environment worldwide in the last decades. The most important origin of NO_x is the combustion of fossil energy sources like coal, natural gas, oil and fuel. In the combustion process, NO is the primary product oxidised, subsequently into NO_2 in atmospheric air. The preferred way to minimise the output of NO_x is the optimisation of the combustion process. Despite this, catalytic abatement technologies are more and more required to meet current and future legislation limits.

For the pollution control of gasoline cars, three way catalysts (TWC) comprising Pt/Rh or Pd/Rh are applied since the 1980s. TWC simultaneously abate NO_x, HC and CO and operate efficiently close to stoichiometric air/fuel ratio [1,2]. Although the reaction network of TWC is complex, the elementary processes are currently well understood [3]. Exemplarily, H_2 considerably contributes to NO_x reduction following the overall equation $2\,NO + 2H_2 \rightarrow N_2 + 2H_2O$. In this concern, the NO–H_2 reaction was widely investigated for Pt, Pd and Rh catalysts, mostly in the absence of O_2 [4–6].

Furthermore, from oxygen-rich exhaust gases reflecting diesel engines, fossil power plants and waste combustion plants HC and CO can simply be removed by using Pt or Pd catalysts [1,7,8]. However, for the efficient reduction of NO_x, additional procedures are required. The classical lean deNO_x technique is the selective catalytic reduction by NH_3 (SCR) already introduced since the 1970s in fossil power plants. The most common SCR catalyst used today is $V_2O_5/WO_3/TiO_2$ [1,2,6,7], whereas for automotive exhaust Fe and Cu based zeolites are lately employed due to their advanced activity and thermal stability [9–13]. Additionally, in lean exhaust of passenger cars NO_x storage reduction catalysts (NSR) are also applied consisting of Pt, Pd and Rh as well as NO_x traps such as Al_2O_3, CeO_2 and $BaCO_3$. The operation of NSR is based on the periodic storage and reduction of NO_x [14,15]. The reduction is performed under rich conditions temporarily induced by engine management and is enhanced by the reaction of NO_x with H_2 on the precious metals components [16,17].

Moreover, the NO_x reduction by H_2 occurs effectively even in excess of O_2. A recent review reports considerable performance of precious metals [18], whereas Pt is highly active already at low temperatures (below 175 °C) being potentially relevant for automotive deNO_x [19]. SCR and NSR start operating above this temperature only. But as a constraint of lean H_2–deNO_x, the hydrogen mainly reacts with the excessive O_2 resulting in low

* Corresponding author. Tel.: +49 3731 39 4482; fax: +49 3731 39 4555.
E-mail address: kureti@iec.tu-freiberg.de (S. Kureti).

http://dx.doi.org/10.1016/j.apcatb.2014.12.033
0926-3373/

H_2 selectivity towards NO_x reduction. Another issue is the pronounced production of N_2O on most Pt, Ir, Rh and Pd catalysts [16]. However, $Pt/La_{0.7}Sr_{0.2}Ce_{0.1}FeO_3$ [20,21] and $Pt/MgO–CeO_2$ [22–24] were lately demonstrated to reveal substantially increased selectivity of N_2. Additionally, we reported on $Pt/WO_3/ZrO_2$ showing marked lean H_2–deNO_x between 50 and 450 °C and high N_2 selectivity up to 90% [25]. For comparison, classical Pt/Al_2O_3 performs only from 50 to 150 °C with a N_2O selectivity of about 80%. $Pt/WO_3/ZrO_2$ also implies outstanding hydrothermal stability as well as resistance against SO_x. Related $Pd/WO_3/ZrO_2$ catalysts even show selective formation of N_2, but their activity is limited to a narrow operation window [26]. High activity and N_2 selectivity are also evidenced for $LaCoO_3$—supported Pd [27], while an enhancing effect of H_2 is highlighted for NO_x reduction by hydrocarbons (lean HC–SCR) using Ag/Al_2O_3 catalysts [28–30].

In situ, spectroscopic studies of the $H_2–O_2–NO_x$ reaction on $Pt/WO_3/ZrO_2$ [25] suggest that the conversion is in accordance with the mechanism widely accepted for Pt catalysts [3,16,31]. This pathway involves the adsorption of NO on reduced Pt sites followed by dissociation into chemisorbed N and O atoms. The recombination of two adjacent N species finally leads to N_2, whereas N_2O is produced by reaction of an N atom with NO both adsorbed on neighbouring Pt sites. NO_x surface species formed on the support are not supposed to be predominately involved in lean H_2–deNO_x on $Pt/WO_3/ZrO_2$. Such a mechanism is proposed for $Pt/La_{0.7}Sr_{0.2}Ce_{0.1}FeO_3$ [21] and $Pt/MgO–CeO_2$ [22].

The objective of this paper is to advance the understanding of the lean $H_2–O_2–NO_x$ reaction on $Pt/WO_3/ZrO_2$. For this purpose, we performed kinetic investigations to construct a kinetic mean field model based on elementary reactions. Finally, the kinetic model was validated by comparing experiments and predictions as well as checking thermodynamic consistency of the kinetic parameters modelled.

2. Experimental

2.1. Preparation and characterisation of the catalyst

The preparation and characterisation of the $Pt/WO_3/ZrO_2$ catalyst were reported recently. Thus, only a brief description is given here [25]. The tetragonal ZrO_2 substrate was obtained by hydrazine synthesis with final calcination in air at 750 °C for 6 h. The introduction of WO_3 and Pt was successively performed by using the incipient wetness impregnation method. The ZrO_2 substrate was treated with an aqueous solution of $(NH_4)_6H_2W_{12}O_{41}$ (Fluka), and after overnight drying Pt was added by taking an aqueous $Pt(NO_3)_2$ solution (Chempur). The sample was activated at 300 °C in a flowing mixture of 9 vol% H_2 and 91 vol% N_2 and was finally conditioned in static air at 500 °C for 5 h. The content of Pt amounted to 0.3%, whereas that of W was 11% both referring to bare ZrO_2 carrier. The BET surface area of $Pt/WO_3/ZrO_2$ was about 70 m^2/g. Pt revealed a dispersion of 90%, while WO_3 existed in the form of nano-scaled particles as well as larger amorphous entities [25].

For the kinetic studies, a commercial cordierite honeycomb with a cell density of 400 cpsi was coated with the catalyst at Umicore company (Hanau). The resulting load of $Pt/WO_3/ZrO_2$ amounted to 100 g/l.

2.2. Kinetic studies

Kinetic studies were performed by using a gradient-free loop reactor with external gas cycle (MZ2C pump, Vacuubrand) [32]. The measurements were made by using a cylindrical core (d = 10 mm, l = 5 mm) taken from the coated monolith. The honeycomb was packed into the quartz glass tube of the reactor, fixed with quartz wool and then the feed was added. The total volumetric flow (F) was 500 ml/min (STP) with a recycle ratio ψ ($\psi = F_{loop}/F_{out}$) of 80. The gas hourly space velocity (GHSV) was 77,000 h^{-1}. As checked by tracer experiments, the residence time behaviour of the reactor corresponded well to that of a continuous stirred tank reactor (CSTR).

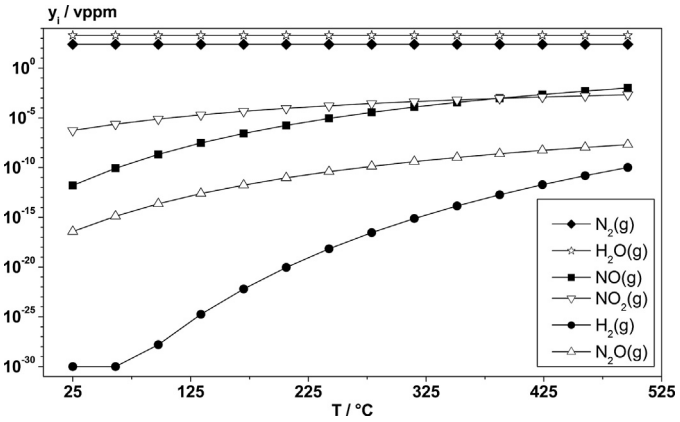

Fig. 1. Equilibrium composition of the $H_2–O_2–NO_x$ reaction; reaction mixture: $y(NO)$ = 500 vpppm, $y(H_2)$ = 2000 vppm, $y(O_2)$ = 5 vol%, Ar balance.

The feed was a blend of pure components (Air Liquide) dosed from independent flow controllers (Bronkhorst) and consisted of H_2, O_2 and NO balanced by N_2. Additionally, some measurements were also made in the absence of NO to study the kinetics of the $H_2–O_2$ reaction independently. The temperature was monitored by two K-type thermocouples located directly in front of and behind the honeycomb. The maximum difference of inlet and outlet temperature was found to be 8 K. The simultaneous analyses of NO, NO_2, N_2O, NH_3, and H_2O was carried out by a hot measuring FTIR spectrometer (MULTI-GAS Analyzer 2030, MKS Instruments). O_2 was monitored by a lambda probe (LSU 4.9, Bosch). The reactor effluents were recorded after reaching steady state; no oscillating behaviour of the $Pt/WO_3/ZrO_2$ catalyst was found in all experiments [33].

3. Results and discussion

3.1. Thermodynamics of the $H_2–O_2–NO_x$ reaction

The thermodynamics of the lean H_2–deNO_x reaction were calculated by HSC Thermodynamic Software 5.1 from Outokumpu. The results are exemplarily shown in Fig. 1 for a reaction mixture composed of 500 vppm NO, 2000 vppm H_2 and 5 vol% O_2 balanced by Ar implying the chemical equilibrium of NO, NO_2, N_2O, N_2, O_2, H_2 and H_2O. The equilibrium composition evidences that N_2 and H_2O are clearly the favoured products, whereas N_2O is only present in negligible amounts.

3.2. Kinetic modelling

For the construction of the kinetic model of lean H_2–deNO_x we followed a stepwise approach. In the first step, the catalytic reaction of H_2 with O_2 was separately investigated. This was done to reduce the number of free parameters in the numeric modelling and to study the kinetics independently, since the H_2 oxidation is significantly affected by the presence of NO as will be shown in Section 3.2.3. In the second step, the NO_x reduction was implemented into the model of the $H_2–O_2$ reaction including the formation of N_2 and N_2O. The conversions are described by a set of elementary reactions implying forward and backward reactions (Eqs. (1)–(6) and (31)–(35)). In theses reaction equations, the free Pt sites considered as the catalytically active sites [3,16,25,32,34] are labelled

by an asterisk (∗). Furthermore, the mean field approximation is employed supposing equivalence of the active Pt sites [3,7,34].

Limitation of the catalytic conversions by film and pore diffusion are excluded by checking Mears Weisz Prater criterion [35], and analysing Arrhenius plots.

3.2.1. Kinetic modelling of the H_2–O_2 reaction

The kinetic model of the H_2 oxidation on $Pt/WO_3/ZrO_2$ is expressed by Eqs. (1)–(6) implying 4 surface species, 3 gas-phase species and 6 reaction steps according to the literature [34,36–38]. This model includes the dissociative adsorption and desorption of H_2 (Eq. (1)) and O_2 (Eq. (2)) as well as the molecular adsorption and desorption of H_2O (Eq. (6)). Additionally, two parallel routes of catalytic H_2O formation are considered including the combination of OH and H and the reaction of OH surface species (Eqs. (3)-(5)). Gas-phase reactions do not play a role under the present reaction conditions as checked by preliminary experiments.

$$H_2(g) + 2^* \underset{r_2}{\overset{r_1}{\rightleftarrows}} 2H* \quad (1)$$

$$O_{2(g)+2^*} \underset{r_4}{\overset{r_3}{\rightleftarrows}} 2O* \quad (2)$$

$$H* + O^* \underset{r_6}{\overset{r_5}{\rightleftarrows}} OH* + * \quad (3)$$

$$H* + OH^* \underset{r_8}{\overset{r_7}{\rightleftarrows}} H_2O* + O* \quad (4)$$

$$2OH^* \underset{r_{10}}{\overset{r_9}{\rightleftarrows}} H_2O* + O* \quad (5)$$

$$H_2O^* \underset{r_{12}}{\overset{r_{11}}{\rightleftarrows}} H_2O(g) + * \quad (6)$$

For every reaction, an Arrhenius-based rate expression is used (Eqs. (7)–(18)), where A_i is the pre-exponential factor and E_i the activation energy. It should be pointed out that for H_2 adsorption (Eq. (7)), the reaction order of Θ_* is assumed to be unity due to very fast diffusion of H and H_2, reducing the effect of the number of unoccupied Pt sites on the adsorption rate [34]. Furthermore, $E_2(0)$ and $E_4(0)$ are the activation energies for desorption of H_2 and O_2 at zero coverage, while the respective correction factor α_i implies linear dependency of $E_i(0)$ on the coverage (θ_i) due to repulsive interactions of the surface species [39–42].

$$r_1 = A_1 \exp\left(-\frac{E_1}{RT}\right) c_{H_2} \Theta_*^2 \quad (7)$$

$$r_2 = A_2 \exp\left(-\frac{E_2(0) - \alpha_2 \Theta_H}{RT}\right) \Theta_H^2 \quad (8)$$

$$r_3 = A_3 \exp\left(-\frac{E_3}{RT}\right) c_{O_2} \Theta_*^2 \quad (9)$$

$$r_4 = A_4 \exp\left(-\frac{E_4(0) - \alpha_4 \Theta_O}{RT}\right) \Theta_O^2 \quad (10)$$

$$r_5 = A_5 \exp\left(-\frac{E_5}{RT}\right) \Theta_O \Theta_H \quad (11)$$

$$r_6 = A_6 \exp\left(-\frac{E_6}{RT}\right) \Theta_{OH} \Theta_* \quad (12)$$

$$r_7 = A_7 \exp\left(-\frac{E_7}{RT}\right) \Theta_{OH} \Theta_H \quad (13)$$

$$r_8 = A_8 \exp\left(-\frac{E_8}{RT}\right) \Theta_{H_2O} \Theta_* \quad (14)$$

$$r_9 = A_9 \exp\left(-\frac{E_9}{RT}\right) \Theta_{OH}^2 \quad (15)$$

$$r_{10} = A_{10} \exp\left(-\frac{E_{10}}{RT}\right) \Theta_{H_2O} \Theta_O \quad (16)$$

$$r_{11} = A_{11} \exp\left(-\frac{E_{11}}{RT}\right) \Theta_{H_2O} \quad (17)$$

$$r_{12} = A_{12} \exp\left(-\frac{E_{12}}{RT}\right) c_{H_2O} \Theta_* \quad (18)$$

The numeric modelling is based on the stationary CSTR mass balance accounting for the gas-phase (Eq. (19)) and adsorbed species (Eq. (20)). ν_{ij} denotes the respective stoichiometric coefficient, A_{act} the active Pt surface and Γ the surface concentration of active sites ($\Gamma = 2.05 \times 10^{-5}$ mol m^{-2} [43,44]), which was simply derived from Pt dispersion, the amount of Pt and the catalyst surface area.

$$\frac{dc_i}{dt} = 0 = F \times \left(c_{i,in} - c_{i,out}\right) + A_{act} \times \sum_{\substack{i=1 \\ i \neq j}}^{n} \nu_{ij} r_j \quad (19)$$

$$\frac{d\Theta_i}{dt} = 0 = \frac{1}{\Gamma} \times \sum_{\substack{i=1 \\ i \neq j}}^{n} \nu_{ij} r_j \quad (20)$$

To reduce the number of free parameters in the fitting procedure, some kinetic parameters are adopted from the literature, while the pre-exponential factors of the adsorption of H_2 (A_1) and O_2 (A_3) are estimated based on the kinetic gas theory (Eq. (21)); N_A is the Avogadro number, R the molar gas constant, M_i the molar mass of the gas species, a_m the surface area per Pt site ($a_m = 6.03 \times 10^{-20}$ m^2 site^{-1}) calculated from the atomic radius of Pt ($r_a = 1.385 \times 10^{-10}$ m [45]) and S^0 is the sticking coefficient for zero coverage [44,46]. The sticking coefficients are taken from the literature; for O_2 S^0 is 0.07, for H_2 0.046 and for H_2O it is 0.75 [34,43,46]. In the calculations, the temperature dependency of A_i is neglected, i.e. A_i is determined for 70 °C representing a mean temperature in the kinetic studies.

$$A_i = \frac{N_A RT}{(2\Pi M_i RT)^{1/2}} a_m \Gamma S^0 \quad (21)$$

Furthermore, the adsorption steps are assumed to occur non-activated, i.e. $E_1 = E_3 = E_{12} = 0$ kJ mol^{-1} being in good agreement with the literature [34,47]. The kinetic parameters for desorption of O_2 (A_4, $E_4(0)$, α_4) are elucidated from kinetic reinvestigation of the pattern of the temperature programmed O_2 desorption on $Pt/WO_3/ZrO_2$ taken from our previous paper [25] providing slightly different kinetic parameters only. Furthermore, $E_2(0)$ and α_2 are adopted from related Pt catalysts [34], while the kinetic parameters of the backward reactions of Eqs. (3)–(5) (A_6, E_6, A_8, E_8, A_{10} and E_{10}) as well as the activation energy for water desorption (E_{11}) is calculated from the thermodynamic equilibrium using NASA polynomials [34,48]. Finally, the remaining parameters, A_2, A_5, A_7, A_9 A_{11}, E_5, E_7 and E_9 are numerically fitted using the Matlab tool lsqcurvefit (nonlinear regression). The temperature depending surface coverages are calculated with the Matlab solver ode15s. For the fits, two sets of experimental data are simultaneously taken referring to different feed compositions ($y(H_2) = 2300$ vppm,

Table 1
Kinetic parameters of the model of the H_2–O_2 reaction on $Pt/WO_3/ZrO_2$.

Parameter	Value	Tolerance[a]	Unit	Reference
A_1	16.1		[m s^{-1}]	Calculated[b]
E_1	0		[kJ mol^{-1}]	[34]
A_2	4.0×10^{11}		[mol (m^2 s)$^{-1}$]	Numerical fit
$E_2(0)$	69.11		[kJ mol^{-1}]	[34]
α_2	6		[kJ mol^{-1}]	[34]
A_3	8.1		[m s^{-1}]	Calculated[b]
E_3	0		[kJ mol^{-1}]	[34]
A_4	1.2×10^{10}	$\pm 1.0 \times 10^{10}$	[mol (m^2 s)$^{-1}$]	Numerical fit
$E_4(0)$	182.6	±5.6	[kJ mol^{-1}]	Numerical fit
α_4	61.9	±3.5	[kJ mol^{-1}]	Numerical fit
A_5	1.2×10^{11}		[mol (m^2 s)$^{-1}$]	Numerical fit
E_5	84		[kJ mol^{-1}]	Numerical fit
A_6	3.2×10^{11}		[mol (m^2 s)$^{-1}$]	Calculated[c]
E_6	144.1		[kJ mol^{-1}]	Calculated[c]
A_7	7.4×10^{14}		[mol (m^2 s)$^{-1}$]	Numerical fit
E_7	56.4		[kJ mol^{-1}]	Numerical fit
A_8	1.3×10^{14}		[mol (m^2 s)$^{-1}$]	Calculated[c]
E_8	106.5		[kJ mol^{-1}]	Calculated[c]
A_9	1.8×10^{4}		[mol (m^2 s)$^{-1}$]	Numerical fit
E_9	57.4		[kJ mol^{-1}]	Numerical fit
A_{10}	1.2×10^{4}		[mol (m^2 s)$^{-1}$]	Calculated[c]
E_{10}	47.3		[kJ mol^{-1}]	Calculated[c]
A_{11}	8.6×10^{12}		[mol (m^2 s)$^{-1}$]	Numerical fit
E_{11}	40.8		[kJ mol^{-1}]	Calculated[c]
A_{12}	87.3		[m s^{-1}]	Calculated[b]
E_{12}	0		[kJ mol^{-1}]	[34]

[a] 95% confidence interval.
[b] Calculated with Eq. (21).
[c] Calculated from thermodynamic constraints.

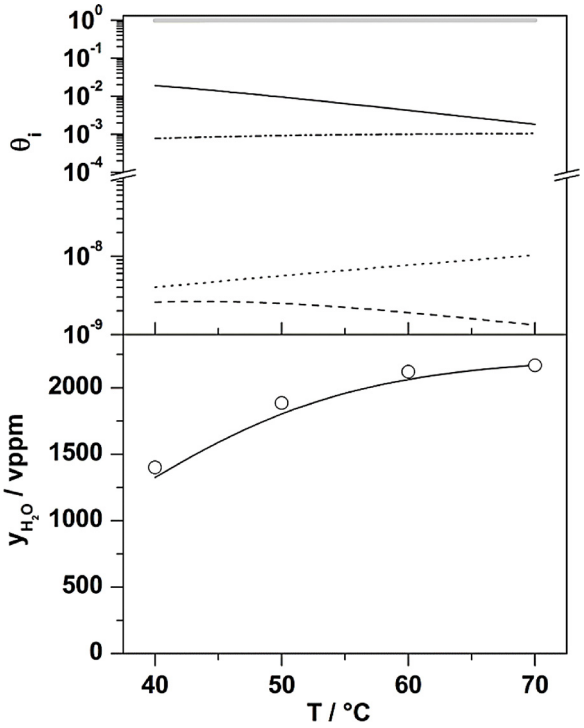

Fig. 6. Experimental (○) and simulated H_2O fraction (—, $R^2 = 0.96$) as well as simulated coverages of $Pt/WO_3/ZrO_2$ by O∗ (–), H∗ (–), OH∗ (· · ·), H_2O∗ (—) and vacant Pt sites (– · · · –) in H_2 oxidation. Conditions: $y(H_2) = 2300$ vppm, $y(O_2) = 6$ vol%, balance N_2, GHSV = 77,000 h^{-1}.

$y(O_2) = 3$ vol% and $y(H_2) = 2300$ vppm, $y(O_2) = 4$ vol%). Since the fitting procedure is carried out based on 8 experimental data points, the 95% confidence interval is not meaningful to assess the accuracy of the kinetic parameters calculated. Thus, the corresponding R^2 parameters $\left(R^2 = 1 - \sum_{i=1}^{n} \left(y_{i,\mathrm{exp}} - y_{i,\mathrm{model}}\right)^2 / \left(y_{i,\mathrm{exp}} - \bar{y_{\mathrm{exp}}}\right)^2\right)$ are taken.

Fig. 2 evidences that the experimental H_2O content is well described by the model and the kinetic parameters implemented therein (Table 1). The accuracy of the fitting is reflected by the high R^2 parameters being close to 1. Furthermore, the simulated surface coverage (Fig. 3) indicated chemisorbed O to be the prevailing surface species with minor abundance of H∗. The remaining species are present in negligible surface concentrations, which is in line with the literature [34,44]. The calculated activation energy of O_2 desorption at zero coverage ($E_4(0) = 182.6$ kJ mol^{-1}) is close to that of Pt catalysts reported in the literature, i.e. 200 kJ mol^{-1} [41] and 213 kJ mol^{-1} [49], respectively. The determined activation energy for H_2O desorption ($E_{11} = 40.8$ kJ mol^{-1}) is also close to literature data. Deutschmann et al. specifies values of 40.3 kJ mol^{-1} [34] and 49.2 kJ mol^{-1} [47]. Warnatz et al. reported a slightly higher activation energy for desorption of water (62.8 kJ mol^{-1}) [37]. The fitted values of the activation energies for the surface reactions shown in Eqs. (3)-(5) (E_5–E_{10}) are higher than corresponding data reported for the H_2 oxidation on Pt catalysts. The activation energy for the formation of OH surface groups by Eq. (3) (E_5) is shown to be to 70 kJ mol^{-1} [47] and 11.5 kJ mol^{-1} [34] (this work: 84 kJ mol^{-1}). E_7 is specified with 17.4 kJ mol^{-1} (this work: 56.4 kJ mol^{-1}) and E_9 with 48.2 kJ mol^{-1} (this work: 57.4 kJ mol^{-1}), respectively [34,47]. It may be noticed, that the different activation energies of model and literature are attributed to the different composition of the catalysts and are considered to be reasonable due to specific interaction of Pt with respective substrate. For example, the data of Deutschmann et al. are referred to a polycrystalline Pt foil [34,38], while that from Koop et al. are associated with Pt/γ–Al_2O_3 catalysts [47]. Additionally, also some effect might also be assigned to the different size of the Pt particles as discussed in Section 3.2.4.

Furthermore, from the kinetic analysis, it is deduced that the dissociative adsorption of O_2 (Eq. (2)) is the rate determining step of the H_2 oxidation on $Pt/WO_3/ZrO_2$. This conclusion is in line with the literature addressing traditional Pt catalysts [34]. The kinetic model also evidences that adsorbed water is preferentially produced by the reaction of OH∗ with H∗ (Eq. (4)), whereas the competitive route by two OH∗ species contributes to minor extent only (Eq. (5)).

3.2.2. *Validation of the kinetic model of the H_2–O_2 reaction*

For validation of the kinetic model, the remaining kinetic measurements are simulated implying O_2 variation from 0.5 to 5 vol%. The simulations are performed based on Eqs. (19) and (20) using the respective experimental conditions as well as the kinetic parameters presented in Table 1. Figs. 4–6 show that the experimental H_2O formation is well described by the simulations as demonstrated by the high R^2 parameters. The maximum difference between experimental and calculated data amounts to 5% only. Furthermore, the kinetic model shows that regardless of the feed content of O_2 the Pt sites are mainly covered by O∗, while other surface groups (H∗, OH∗ and H_2O∗) are present in little quantity. It is also worth noting that unoccupied Pt sites are still available, although the temperatures are rather low potentially favouring adsorption processes.

For further validation, the thermodynamic consistency of the kinetic parameters implemented into the elementary kinetic model is also evaluated [50]. Calorimetric studies from Yeo et al. indicate that at 20 °C the enthalpy of the dissociative chemisorption of O_2 on Pt(1 1 1) lies in the range of about −125 kJ mol^{-1} at steady state [51], whereas another value is reported to be −219 kJ mol^{-1} [34]. With the kinetic model, the adsorption enthalpy is calculated as $\Delta H_{\mathrm{ads}} = E_3 - E_4(0) = -182.6$ kJ mol^{-1} lying in the broad range of above literature data. Furthermore, for the catalytic H_2 oxidation, the reaction enthalpy and reaction entropy are deduced

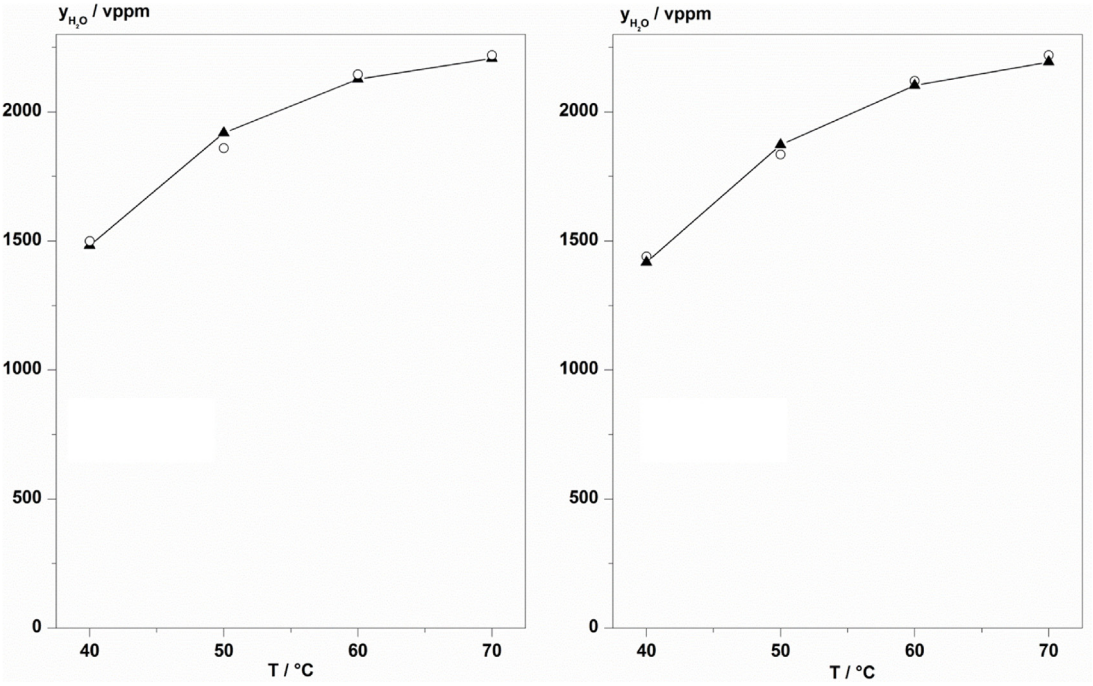

Fig. 2. Experimental (◯) and fitted H_2O fraction (–▲–) in H_2 oxidation on $Pt/WO_3/ZrO_2$ with O_2 fraction of 3 vol% (left, $R^2 = 0.99$) and 4 vol% (right, $R^2 = 0.99$); lines are guides for the eyes. Conditions: $y(H_2) = 2300$ vppm, balance N_2, GHSV = 77,000 h^{-1}.

from Eqs. (22) and (23), respectively, where c_{ij} are factors of linearly decomposed reactions. These coefficients are determined by row echelon reduction of the reaction mechanism [50] following similar calculations presented in [52] expressing the sequence of elementary and linearly independent reactions occurring in the formation of gaseous H_2O. From these mathematical operations, Eq. (24) is obtained for the enthalpy ($\Delta_R H_s$) and Eq. (25) for the entropy ($\Delta_R S_s$) of the catalytic surface reactions. It should be noted that Eq. (5) is a linearly dependent reaction; and is therefore, not considered for the enthalpy and entropy calculations. This approach results in an enthalpy of $\Delta_R H_s = -241.9\ kJ\ mol^{-1}$ being very close to that determined for the enthalpy (Eqs. (26) and (27)) for the gas-phase reaction $H_2(g) + 0.5\ O_2(g) \rightarrow H_2O(g)$ at 70 °C, i.e. $\Delta_R H_g(T = 70\ °C) = -242.5\ kJ\ mol^{-1}$. The thermo-chemical data used

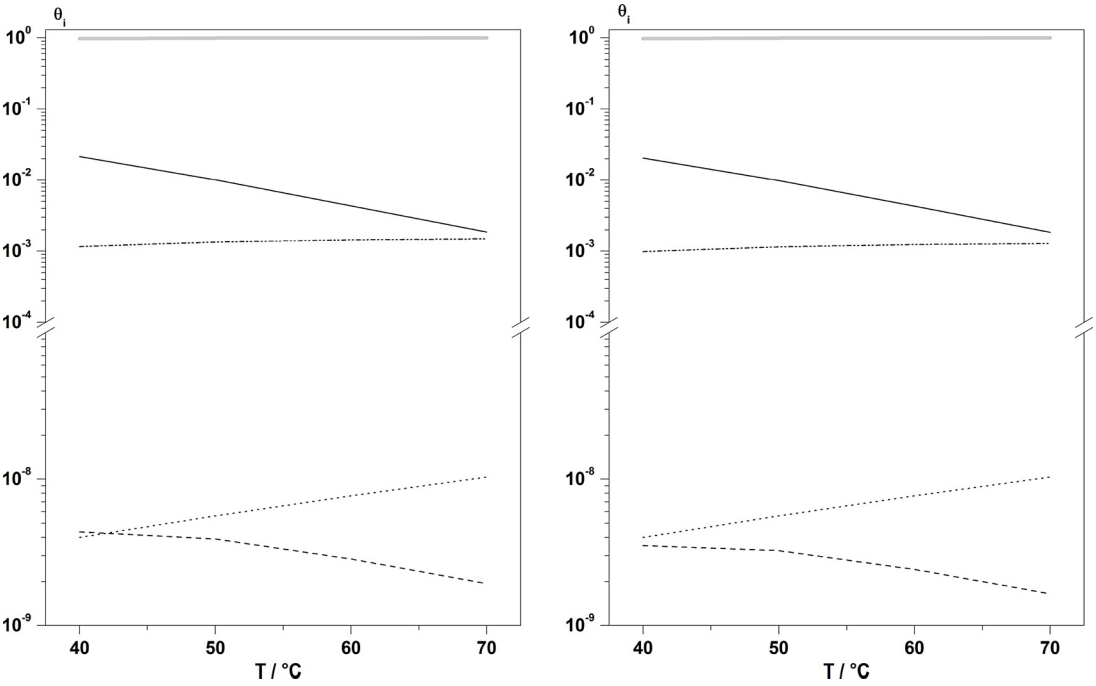

Fig. 3. Simulated coverages of $Pt/WO_3/ZrO_2$ by O∗ (–), H ∗ (–), OH∗ (· · ·), H_2O∗ (—) and vacant Pt sites (– · · –) in H_2 oxidation with O_2 fraction of 3 vol% (left) and 4 vol% (right). Corresponding gas-phase fractions and conditions are demonstrated in Fig. 2.

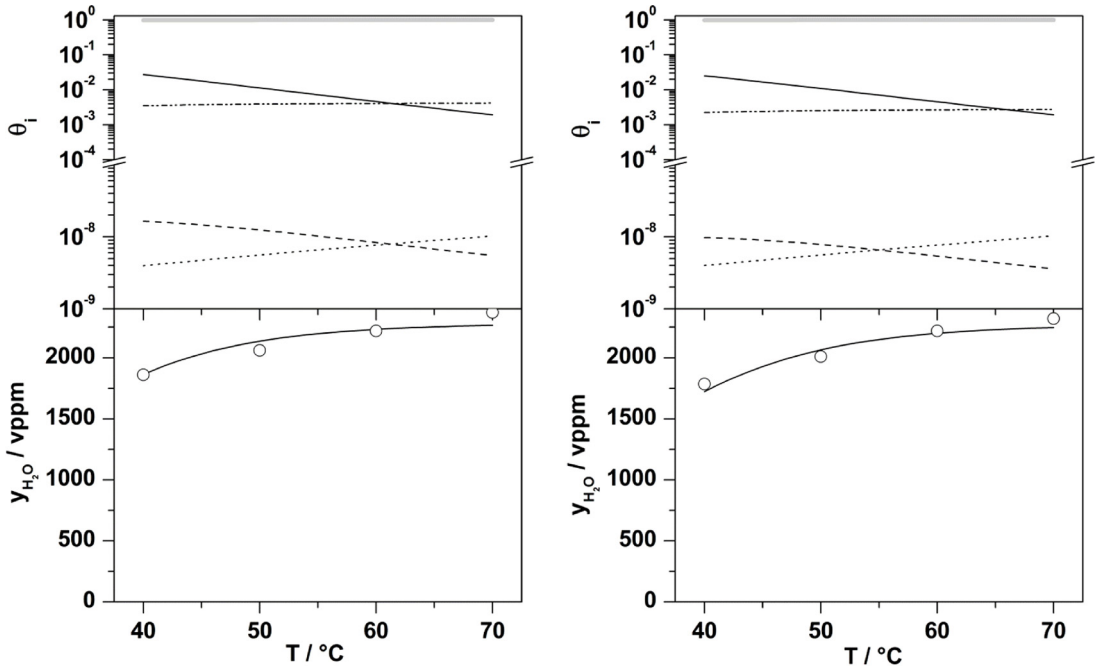

Fig. 4. Experimental (◯) and simulated H_2O fraction (—) as well as simulated coverages by O∗ (–), H∗ (–), OH∗ (· · ·), H_2O∗ (—) and vacant Pt sites (– · · –) in H_2 oxidation on $Pt/WO_3/ZrO_2$ with O_2 fraction of 0.5 vol% (left, $R^2 = 0.88$) and 1 vol% (right, $R^2 = 0.93$). Conditions: $y(H_2) = 2300$ vppm, balance N_2, GHSV = 77,000 h^{-1}.

for the calculation of $\Delta_R H_g$ (Eqs. (26) and (27)) are taken from the literature [53].

$$\Delta_R H_s = \sum_{\substack{i=1 \\ i \neq j}}^{n} c_{ij} \left(E_j^f - E_j^b \right) \tag{22}$$

$$\Delta_R S_s = R \ln \prod_{\substack{i=1 \\ j \neq n}}^{n} \left(\frac{A_j^f}{A_j^b} \right) c_{ij} \tag{23}$$

$$\Delta_R H_s = (E_1 - E_2(0)) + 0.5(E_3 - E_4(0)) + (E_5 - E_6) + (E_7 - E_8) + (E_{11} - E_{12}) \tag{24}$$

$$\Delta_R S_s = R \ln \left(\frac{A_1}{A_2} \left(\frac{A_3}{A_4} \right) 0.5 \frac{A_5}{A_6} \frac{A_7}{A_8} \frac{A_{11}}{A_{12}} \right) \tag{25}$$

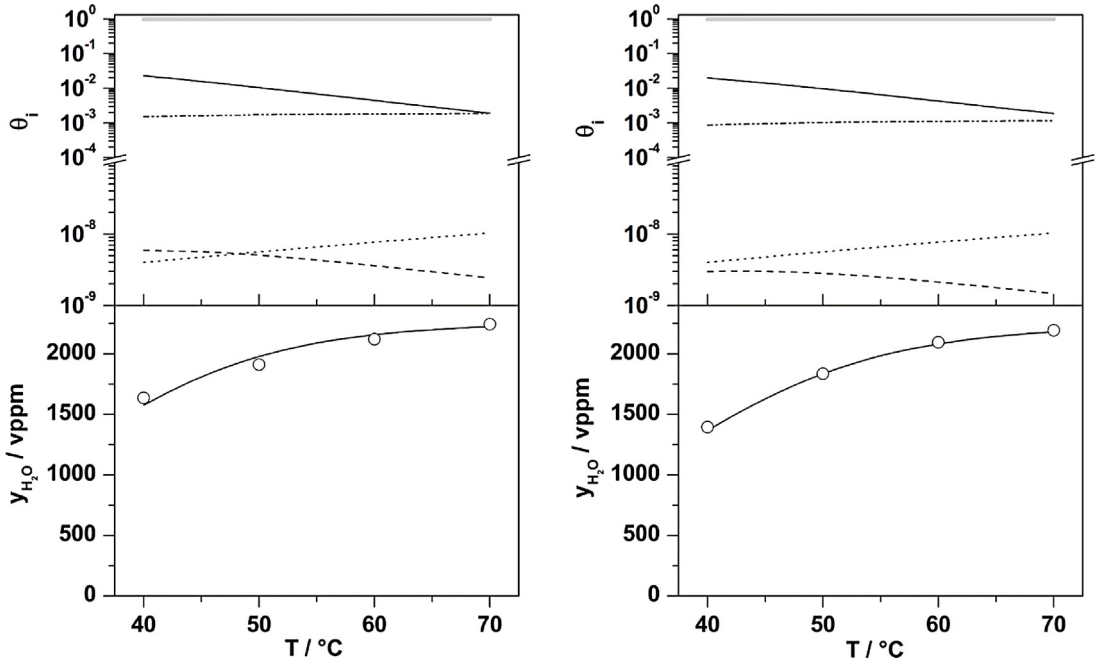

Fig. 5. Experimental (◯) and simulated H_2O fraction (—) as well as simulated coverages of $Pt/WO_3/ZrO_2$ by O∗ (–), H∗ (–), OH∗ (· · ·), H_2O∗ (—) and vacant Pt sites (– · · –) in H_2 oxidation with O_2 fraction of 2 vol% (left, $R^2 = 0.95$) and 5 vol% ($R^2 = 0.99$). Conditions: $y(H_2) = 2300$ vppm, balance N_2, GHSV = 77,000 h^{-1}.

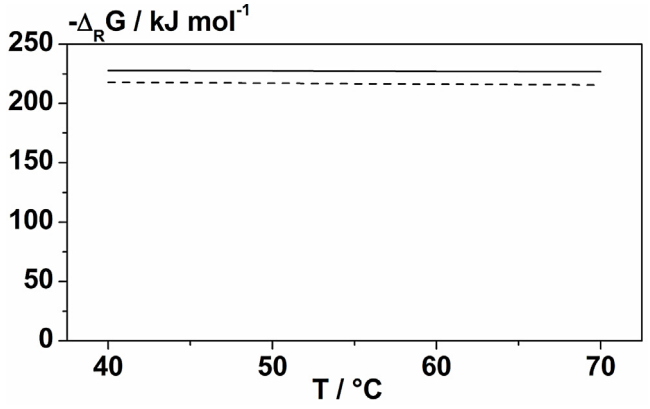

Fig. 7. Gibbs free enthalpy of the H_2 oxidation ($H_2(g) + 0.5\,O_2(g) \rightarrow H_2O(g)$) calculated with thermochemical data (—) and kinetic parameters of the surface reaction on $Pt/WO_3/ZrO_2$ (- - -).

$$\Delta_R H_g(T) = \sum_{\substack{i=1 \\ i \neq j}}^{n} \nu_{ij} H_{g,i}(T) \tag{26}$$

$$H_{g,i}(T) = H_{g,i}(T_0) + \int_{T_0}^{T} c_{p,i}\,dT \tag{27}$$

From the kinetic parameters, a reaction entropy of $\Delta_R S_s = -77\,J\,(mol\,K)^{-1}$ is calculated, which is close to that derived from thermochemistry (Eqs. (28) and (29)) [53]. For instance at 70 °C, $\Delta_R S_g$ is equal to $-45.9\,J\,(mol\,K)^{-1}$. Moreover, the Gibbs free enthalpy is also determined for the catalytic surface and gas-phase reaction (Eq. (30)). The results display very good accordance of both values in the whole temperature range implying a difference of ca. 5% only (Fig. 7). As a consequence, the model of the H_2 oxidation on $Pt/WO_3/ZrO_2$ is assessed to be thermodynamically consistent.

$$\Delta_R S_g(T) = \sum_{\substack{i=1 \\ i \neq j}}^{n} \nu_{ij} S_{g,i}(T) \tag{28}$$

$$S_{g,i}(T) = S_{g,i}(T_0) + \int_{T_0}^{T} \frac{c_{p,i}}{T}\,dT \tag{29}$$

$$\Delta_R G = \Delta_R H - T \times \Delta_R S \tag{30}$$

3.2.3. *Kinetic modelling of the H_2–O_2–NO_x reaction*

The kinetic model of the H_2 oxidation in excess of O_2 is extended by additionally considering the NO reduction to yield N_2 and N_2O. The resulting model includes 6 gaseous and 8 surface species. Based on the mechanism suggested in our recent study, exclusively showing the participation of NO chemisorbed on Pt [25] and in line with literature [3,16,30,47] the model of the H_2–O_2–NO_x reaction on $Pt/WO_3/ZrO_2$ implies the adsorption and desorption of NO (Eq. (31)) and N_2O (Eq. (35)), the formation of N∗ by dissociation of NO∗ (Eq. (32)) and the reaction of NO∗ with H∗ (Eq. (33)). Furthermore, N_2 is assumed to be formed by combination of two N∗ species (Eq. (36)), while N_2O originates from the reaction of N∗ with NO∗ (Eq. (34)). For the reduction of the quantity of free kinetic parameters, our model accounts for the direct genesis of gaseous N_2 from two N∗ species. This simplification is supposed to be justified, since molecular nitrogen is shown not to stick significantly on Pt surfaces above −173 °C [54]. Also, it is reported that produced N_2 promptly desorbs without any formation of stable equilibrated N_2 surface species [55].

$$NO + * \underset{r_{14}}{\overset{r_{13}}{\rightleftharpoons}} N\,O* \tag{31}$$

$$N\,O* + * \underset{r_{16}}{\overset{r_{15}}{\rightleftharpoons}} N* + O* \tag{32}$$

$$NO* + N* \underset{r_{18}}{\overset{r_{17}}{\rightleftharpoons}} N_2O* + * \tag{33}$$

$$N\,O* + N* \underset{r_{20}}{\overset{r_{19}}{\rightleftharpoons}} N_2O* + * \tag{34}$$

$$N_2O + * \underset{r_{22}}{\overset{r_{21}}{\rightleftharpoons}} N_2O* \tag{35}$$

$$2N* \underset{r_{24}}{\overset{r_{23}}{\rightleftharpoons}} N_2 + 2* \tag{36}$$

The mechanism presented above follows the one proposed by Koop and Deutschmann [47]. Very recent work suggested that reduction of NO can also occur by the addition of H∗ to form HNO and HNOH surface intermediates on the active Pt sites [6]. However, this catalytic route is not considered here. The rate expressions corresponding to the reaction mechanism (Eqs. (31)–(36)) are described by Eqs. (37)–(48). Eq. (40) supposes that the activation energy of the formation of NO∗ from N∗ and O∗ linearly depends on the O∗ coverage as expressed by the factor α_{16} (Eq. (40)). $E_{16}(0)$ is the activation energy at zero coverage [47]. Very similar approach is considered for the desorption of H_2 and O_2 (Eqs. (8) and (10)).

$$r_{13} = A_{13}\exp\left(-\frac{E_{13}}{RT}\right) c_{NO}\Theta_*$$ (37)

$$r_{14} = A_{14}\exp\left(-\frac{E_{14}}{RT}\right) \Theta_{NO}$$ (38)

$$r_{15} = A_{15}\exp\left(-\frac{E_{15}}{RT}\right) \Theta_{NO}\Theta_*$$ (39)

$$r_{16} = A_{16}\exp\left(-\frac{E_{16}(0) - \alpha_{16}\Theta_O}{RT}\right) \Theta_N\Theta_O$$ (40)

$$r_{17} = A_{17}\exp\left(-\frac{E_{17}}{RT}\right) \Theta_{NO}\Theta_H$$ (41)

$$r_{18} = A_{18}\exp\left(-\frac{E_{18}}{RT}\right) \Theta_{OH}\Theta_N$$ (42)

$$r_{19} = A_{19}\exp\left(-\frac{E_{19}}{RT}\right) \Theta_{NO}\Theta_N$$ (43)

$$r_{20} = A_{20}\exp\left(-\frac{E_{20}}{RT}\right) \Theta_{N_2O}\Theta_*$$ (44)

$$r_{21} = A_{21}\exp\left(-\frac{E_{21}}{RT}\right) c_{N_2O}\Theta_*$$ (45)

$$r_{22} = A_{22}\exp\left(-\frac{E_{22}}{RT}\right) \Theta_{N_2O}$$ (46)

$$r_{23} = A_{23}\exp\left(-\frac{E_{23}}{RT}\right) \Theta_N^2$$ (47)

Table 2
Kinetic parameters of the model of the NO_x reactions on $Pt/WO_3/ZrO_2$.

Parameter	Value	Unit	Reference
A_{13}	87.6	[m s^{-1}]	Calculated[a]
E_{13}	0	[kJ mol^{-1}]	[47]
A_{14}	5.7×10^5	[mol (m^2 s)$^{-1}$]	Numerical fit
E_{14}	72.4	[kJ mol^{-1}]	Calculated[b]
A_{15}	9.6	[mol (m^2 s)$^{-1}$]	Calculated[b]
E_{15}	86.8	[kJ mol^{-1}]	Calculated[b]
A_{16}	4.7	[mol (m^2 s)$^{-1}$]	Numerical fit
$E_{16}(0)$	72.0	[kJ mol^{-1}]	Numerical fit
α_{16}	31.0	[kJ mol^{-1}]	[47]
A_{17}	7.4e+6	[mol (m^2 s)$^{-1}$]	Numerical fit
E_{17}	72.4	[kJ mol^{-1}]	Numerical fit
A_{18}	4.0×10^7	[m s^{-1}]	Calculated[b]
E_{18}	147.4	[kJ mol^{-1}]	Calculated[b]
A_{19}	22.6	[mol (m^2 s)$^{-1}$]	Numerical fit
E_{19}	43.8	[kJ mol^{-1}]	Numerical fit
A_{20}	6.8×10^4	[mol (m^2 s)$^{-1}$]	Calculated[b]
E_{20}	86.1	[kJ mol^{-1}]	Calculated[b]
A_{21}	2.1	[m s^{-1}]	Calculated[a]
E_{21}	10.8	[kJ mol^{-1}]	Calculated[b]
A_{22}	2.1×10^3	[mol (m^2 s)$^{-1}$]	Numerical fit
E_{22}	0.73	[kJ mol^{-1}]	[47]
A_{23}	8.7×10^{17}	[mol (m^2 s)$^{-1}$]	Numerical fit
E_{23}	163.0	[kJ mol^{-1}]	Numerical fit
A_{24}	2.3×10^{16}	[m s^{-1}]	Calculated[b]
E_{24}	395.6	[kJ mol^{-1}]	Calculated[b]

[a] Calculated with Eq. (21).
[b] Calculated from thermodynamic constraints.

$$r_{24} = A_{24}\exp\left(-\frac{E_{24}}{RT}\right) c_{N_2}\Theta_*^2 \quad (48)$$

The pre-exponential factors of the adsorption of NO (A_{13}) and N_2O (A_{21}) are calculated by using Eq. (21) with $S^0(NO) = 0.85$ and $S^0(N_2O) = 0.025$ [47], while taking 162.5 °C as the mean temperature. The adsorption of NO is considered to be inactivated ($E_{13} = 0$ kJ mol^{-1}), whereas the adsorption of N_2O is supposed as a slightly activated process; the respective value for the activation energy $E_{21} = 10.8$ kJ mol^{-1} is derived from NASA polynomials [47] to ensure thermodynamically consistency. The activation energy of N_2O desorption (E_{19}) as well as α_{16} are adopted from the literature [47]. The kinetic parameters A_{14}, A_{16}, $E_{16}(0)$, A_{17}, E_{17}, A_{19}, E_{19}, A_{22}, A_{23} and E_{23} are numerically fitted, whereas E_{14}, A_{15}, E_{15}, A_{18}, E_{18}, A_{20}, E_{20}, A_{24}, E_{24} are calculated from thermodynamic constraints [48] Table 2.

The fitting calculations are performed based on the mass balances of the gaseous and surface species as described for the H_2 oxidation, while using the rate Eqs. (37)–(48) for the NO_x chemistry. The model of the catalytic H_2–O_2 reaction is coupled into the balance of the surface species by introducing Θ_H, Θ_{OH}, Θ_{H_2O} and Θ_O. For the fitting procedure, the experimental run with 2000 vppm NO_x and 6000 vppm H_2 is taken, whereas the free parameters are numerically adjusted by using the experimental NO_x and N_2O data. The fitted NO and N_2O traces, calculated H_2O proportion and corresponding R^2 parameters are demonstrated in Fig. 8 showing satisfactorily agreement with the experimental data; only for water a slight shift for the light-off is observed. It should be pointed out that due to the relative small number of experimental points, the corresponding R^2 values range from 0.63 and 0.72. The kinetic parameters of the deNO_x reactions are summarised in Table 2.

In the numeric modelling, the activation energy of the NO desorption (E_{14}) is estimated to be 72.4 kJ mol^{-1} being in good agreement with the literature (82 kJ mol^{-1}) [40,44]. Contrary, the activation energy of the N_2O* formation ($E_{19} = 43.8$ kJ mol^{-1}) is clearly lower as referred to literature (ca. 90 kJ mol^{-1}) [43,47,56], whereas the activation energy of the production of N_2 ($E_{23} = 163$ kJ mol^{-1}) is higher than the value published (130 kJ mol^{-1}) [52]. Although the energy barrier of the N_2 genesis is high, this reaction step is still fast associated with the high frequency factor ($A_{23} = 8.7\ 10^{17}$ mol m^{-2} s^{-1}). As a consequence, the production of gaseous N_2 occurs even faster than the nearly inactivated N_2O desorption ($E_{22} = 0.73$ kJ mol^{-1}). Contrary, the dissociative adsorption of N_2 is supposed to be negligible due to its reasonably high activation energy ($E_{24} = 395.6$ kJ mol^{-1}). Moreover, the activation energies of the dissociation of NO* ($E_{15} = 86.8$ kJ mol^{-1}) and the recombination of N* with O* ($E_{16}(0) = 72$ kJ mol^{-1}) are lower as compared to literature indicating values above 100 kJ mol^{-1} [43,47,52]. Also, the kinetic analysis indicates that the major path of the conversion of NO* is the dissociation (Eq. (32)) referring to the high coverage by NO*. In contrast to that, in lean H_2–deNO_x on $Pt/BaO/Al_2O_3$, it is discussed that NO* predominately reacts with adsorbed hydrogen according to Eq. (33) [52].

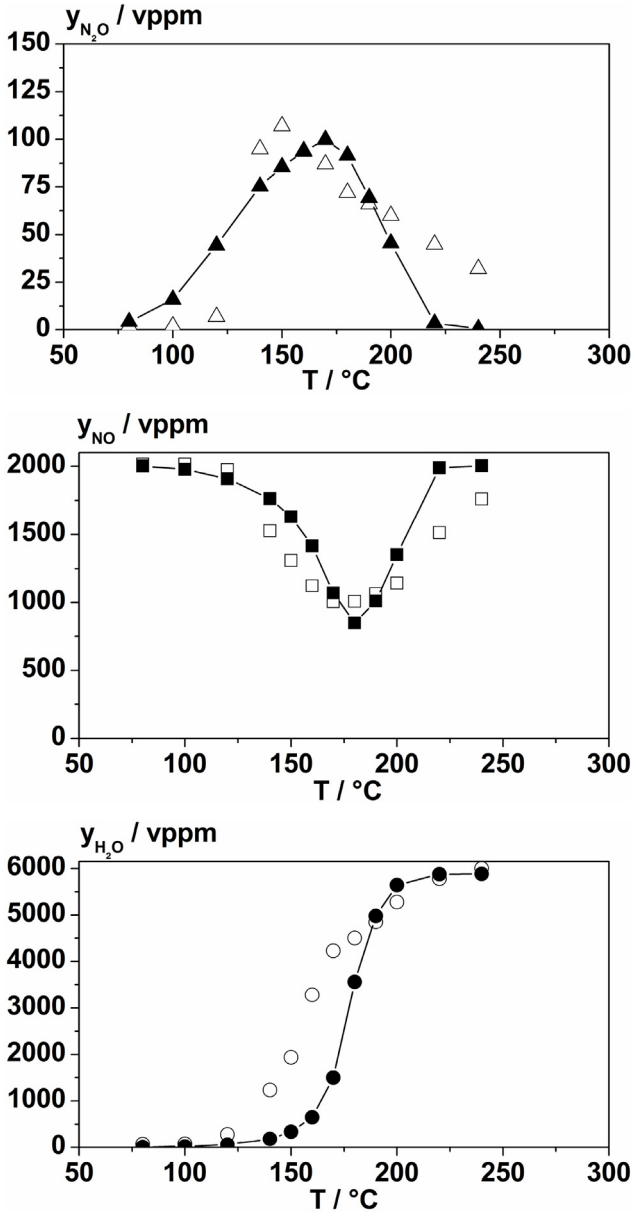

Fig. 8. Fractions of N_2O (Δ experimental, ▲ fitted), NO (□ experimental, ■ fitted) and H_2O (○ experimental, ● simulated) in H_2–O_2–NO_x reaction on $Pt/WO_3/ZrO_2$ (lines are guides for the eyes). Conditions: $y(NO_x) = 2000$ vppm, $y(H_2) = 6000$ vppm, $y(O_2) = 6$ vol%, N_2 balance, GHSV = 77,000 h^{-1}. $R^2(N_2O) = 0.63$, $R^2(NO) = 0.72$, $R^2(H_2O) = 0.67$.

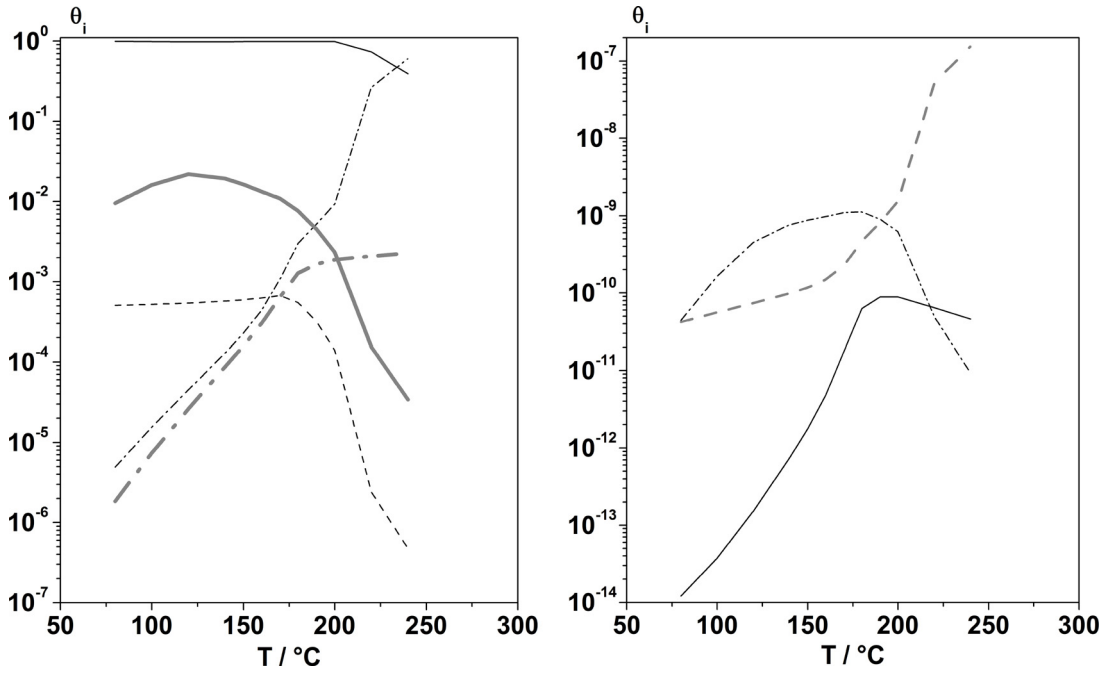

Fig. 9. Simulated coverages of $Pt/WO_3/ZrO_2$ in the H_2–O_2–NO_x reaction. Left: coverages by NO∗ (—), N∗ (–), H∗ (- - -), O∗ (- · -) and free Pt site (- · -); right: coverages by N_2O∗ (- · -), OH∗ (- - -) and H_2O (—). Corresponding gas-phase fractions and conditions are demonstrated in Fig. 8.

Moreover, the modelling also provides simulation of the surface coverage suggesting predominant coverage of the Pt sites by NO at temperatures below 200 °C (Fig. 9). As a consequence, the low oxygen coverage is considered to explain the shift of the H_2 light-off to higher temperatures in the presence of NO. This light-off shift is observed to lie in the range of about 100 K, when NO is supplied. For example, the addition of NO to the feed shifts the H_2O light-off from a temperature below 50 °C (Fig. 2) to ca. 120 °C (Fig. 8 and Figs. 10–12). The relatively high NO surface coverage is in line with in situ DRIFTS studies of $Pt/WO_3/ZrO_2$ performed under very similar reaction conditions showing clear bands of NO coordinated to Pt sites [25]. Furthermore, the simulations indicate rapid decrease in the NO coverage above 200 °C changing the prevailing surface species towards O∗. This probably occurs due to the acceleration of the combination of N∗ and O∗ to NO∗ as well as desorption of NO (backward reactions of Eqs. (31) and (32)), both yielding free adsorption sites for the adsorption of O_2. Additionally, the high coverage by NO below 150 °C substantiates the appreciable formation of the by-product N_2O at low temperatures, as N_2O is produced by the combination of NO∗ and N∗ (Eq. (34)). Hence, the surface concentration of NO obviously drives the rate of N_2O genesis, although N_2O is thermodynamically not favoured under the reaction conditions established (Fig. 1). However, from the analysis of the reaction rates we deduce that the N∗ species are mainly consumed by combination with another N∗ to form N_2 (Eq. (36)) and only to minor proportion by NO∗ yielding N_2O ∗ (Eq. (34)). This interpretation substantiates the high N_2 selectivity of $Pt/WO_3/ZrO_2$ as compared to traditional Pt catalysts, e.g. Pt/Al_2O_3, forming N_2O as major product [25]. For instance, $Pt/WO_3/ZrO_2$ shows a N_2 selectivity of 90% (predicted: 84%) at maximum NO_x conversion, i.e. 160 °C (Fig. 8).

$Pt/WO_3/ZrO_2$ reveals lower energy barrier of the NO dissociation (86.8 kJ mol^{-1} vs. 108 kJ mol^{-1} for Pt/Al_2O_3 [47] and $Pt/BaO/Al_2O_3$ [52]); thus, increasing the coverage by N evoking N_2. It is suggested that the superior formation of N_2 on $Pt/WO_3/ZrO_2$ is associated with the increase of the electron density on the Pt sites by electronic interaction with the WO_3/ZrO_2 substrate as derived from a systematic DRIFTS study of $Pt/WO_3/ZrO_2$, Pt/ZrO_2 and Pt/Al_2O_3 using CO as probe molecule [25].

Another crucial feature of the H_2–O_2–NO_x reaction is the decrease in the NO_x conversion at higher temperatures (Fig. 8). This effect is related to the inclining coverage by O∗ above 200 °C (Fig. 9) drastically decreasing Θ_{NO} and Θ_N (Fig. 9) and suppressing the dissociation of NO∗ (Eq. (32)) as well as combination of N∗ (Eq. (36)). Further, the growth of the oxygen coverage leads to the acceleration of the production of H_2O. The kinetic analysis suggests that the formation of OH∗ (Eq. (3)) represents the rate-limiting step of the genesis of H_2O assigned to the low coverage of H∗.

3.2.4. *Validation of the kinetic model of the H_2–O_2–NO_x reaction*

For validation of the kinetic model, simulations are conducted producing satisfactory prediction of the measured traces of NO_x, N_2O and H_2O as expressed by respective R^2 parameters (Figs. 10–12). As a noticeable feature, the model tends to predict slightly higher N_2O proportions. Exemplarily, for the feed containing 1000 vppm NO, 10,000 vppm H_2 and 6 vol% O_2, the simulation provides formation of 140 vppm N_2O ($S(N_2O) = 16\%$) at 150 °C, whereas the experiment shows 50 vppm only corresponding to a lower N_2O selectivity of 8% (Fig. 12). It should also be noted that below 150 °C, the formation of water is predicted to form slightly slower. The start of the modelled light-off is indicated at 150 °C, whereas in the experiment it is ca. 20 K lower. These deviations are mainly attributed to the lack of kinetic parameters referring to the present $Pt/WO_3/ZrO_2$ catalyst. Furthermore, the structure sensitivity of supported Pt catalysts in the H_2 deNO_x reaction [57] could also affect the kinetics, which was not considered here as a consequence of the mean field approach followed. The majority of kinetic parameters of the H_2–O_2–NO_x model had to be adopted from related Pt catalysts (29 from 51 parameters), which obviously exhibit specific activity and N_2 selectivity. Therefore, the appearing differences are assessed to be intrinsic to the kinetic parameters implemented into the model. Additionally, deviations may also refer to the mean field approximation considering equivalence of the Pt sites. It is known from the literature that the catalytic activity of Pt can depend on particle size [58] and crystalline orientation [59]. Moreover, the surface coverages obtained from the simulations closely resemble that shown in Fig. 9.

Table 3
Reaction enthalpies and entropies of the NO_x reactions at 150 °C derived from thermo-chemical data and kinetic parameters of the catalytic surface model.

Overall reaction	$\Delta_R H$/kJ mol^{-1}		$\Delta_R S$/J (mol K)$^{-1}$	
	Gas-phase	Surface	Gas-phase	Surface
$NO(g)+H_2(g) \rightarrow 0.5\,N_2(g)+H_2O(g)$	−334	−312	−61.4	−33.5
$NO(g)+0{,}5H_2(g) \rightarrow 0.5\,N_2O(g)+0.5H_2O(g)$	−171	−161	−75.0	−65.2
$N_2O(g)+H_2(g) \rightarrow N_2(g)+H_2O(g)$	−325	−304	27.0	63.3

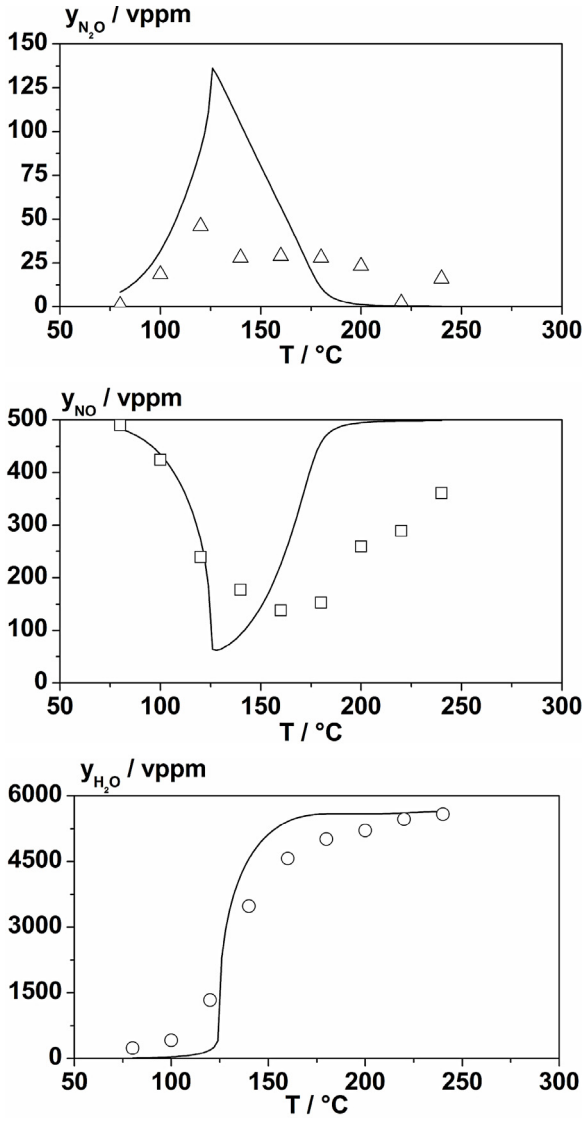

Fig. 10. Experimental fractions of N_2O (Δ), NO (□) and H_2O (○) and corresponding simulated fractions (—) in the H_2–O_2–NO_x reaction on $Pt/WO_3/ZrO_2$. Conditions: $y(NO_x)$ = 500 vppm, $y(H_2)$ = 6000 vppm, $y(O_2)$ = 6 vol%, N_2 balance, GHSV = 77,000 h^{-1}. $R^2(N_2O) = -5.1$, $R^2(NO) = -0.87$, $R^2(H_2O) = 0.90$.

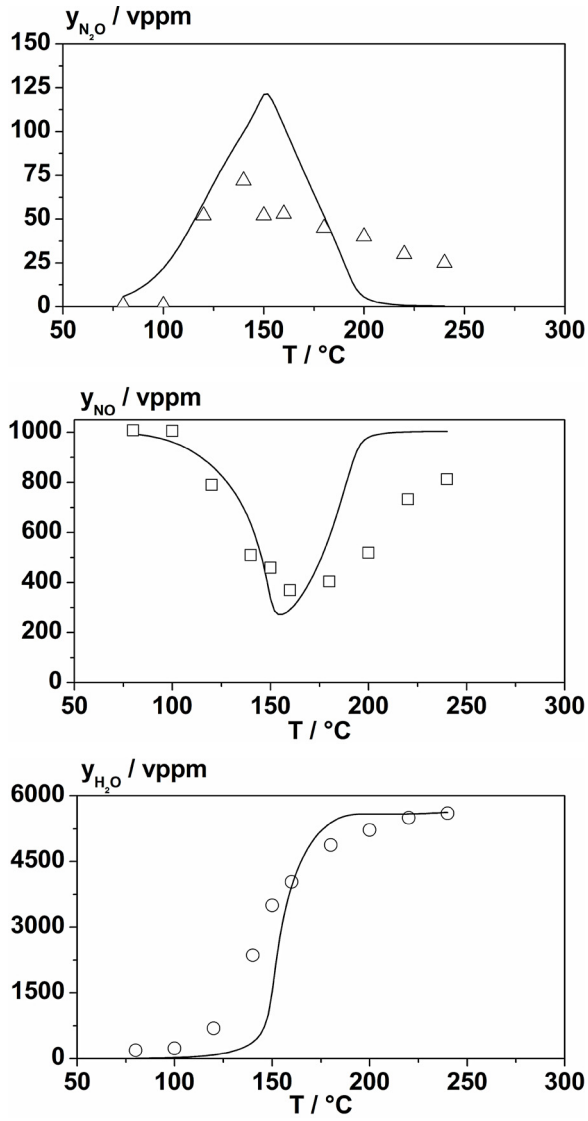

Fig. 11. Experimental fractions of N_2O (Δ), NO (□) and H_2O (○) and corresponding simulated fractions (—) in the H_2–O_2–NO_x reaction on $Pt/WO_3/ZrO_2$. Conditions: $y(NO_x)$ = 1000 vppm, $y(H_2)$ = 6000 vppm, y (O_2) = 6 vol%, N_2 balance, GHSV = 77,000 h^{-1}. $R^2(N_2O) = -1.4$, $R^2(NO) = 0.25$, $R^2(H_2O) = 0.80$.

The thermodynamic consistency of the kinetic model of the H_2–O_2–NO_x reaction is checked as described in Section 3.2.2 (Eqs. (22) and (23)). For this purpose, the reaction enthalpy and entropy of the catalytic pathways are calculated implying the NO decomposition (Eqs. (49) and (50)), N_2O formation (Eqs. (51) and (52)) and N_2O decomposition (Eqs. (52) and (53)) and are compared with the thermo-chemical data of the corresponding gas-phase reactions (Eqs. (26) and (28)), i.e. $NO(g)+H_2(g) \rightarrow 0.5\,N_2(g)+H_2O(g)$, $NO(g)+0.5H_2(g) \rightarrow 0.5\,N_2O(g)+0.5H_2O(g)$ and $N_2O(g)+H_2(g) \rightarrow N_2(g)+H_2O(g)$. The results are demonstrated in Table 3 evidencing only less than 10% difference between the values of the surface and gas-phase reactions. Furthermore, the Gibbs free enthalpy is evaluated for both pathways (Eq. (30)). Fig. 13 displays good agreement of the $\Delta_R G$ values of the gas-phase and catalytic surface reaction in the entire temperature regime. The relative difference is at most 5% only observed for the NO reduction to N_2O (80 °C), while for the NO reduction to N_2 it is 3.6% and for N_2O reduction 2.5%, respectively. Consequently, this comparison indicates thermodynamic accordance of the kinetic parameters. Furthermore, the used reaction mechanism (Eqs. (1)–(6) and (31)–(36)) with its respective kinetic parameters (Tables 1 and 2) is also consistent for the participation of O_2 in the NO reduction [22,60] as exemplarily expressed by

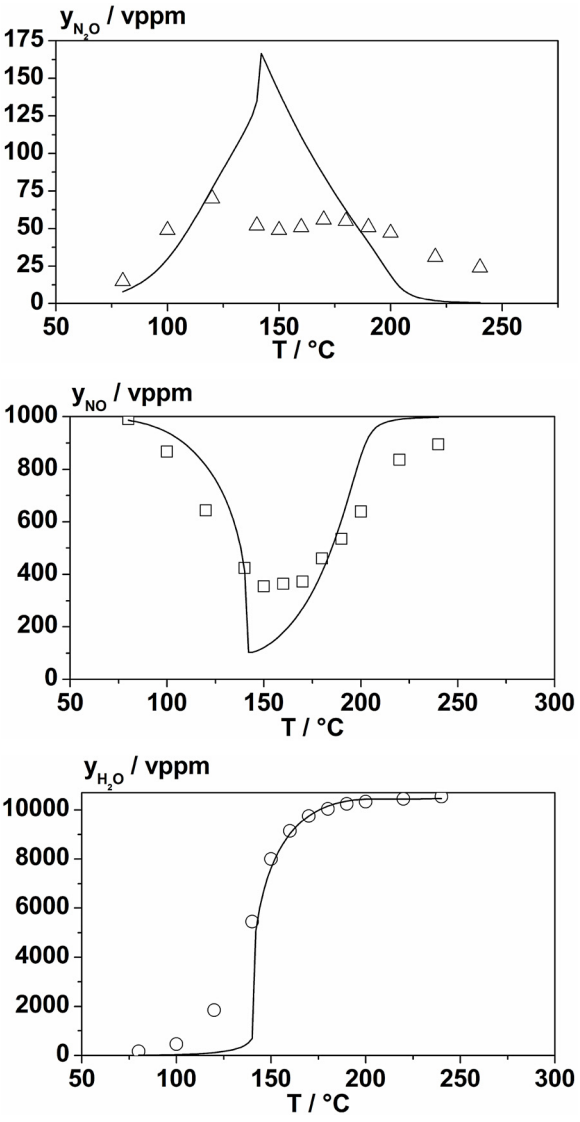

Fig. 12. Experimental fractions of N_2O (Δ), NO (□) and H_2O (○) and corresponding simulated fractions (—) in the H_2–O_2–NO_x reaction on $Pt/WO_3/ZrO_2$. Conditions: $y(NO_x)$ = 1000 vppm, $y(H_2)$ = 10,000 vppm, y (O_2) = 6 vol%, N_2 balance, GHSV = 77,000 h^{-1}. $R^2(N_2O) = -7.9$, $R^2(NO) = 0.56$, $R^2(H_2O) = 0.86$.

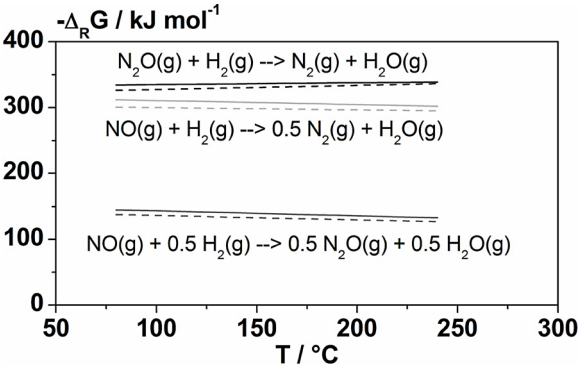

Fig. 13. Gibbs free enthalpy calculated with thermo-chemical data (solid lines) and kinetic parameters of the surface reaction on $Pt/WO_3/ZrO_2$ (dashed lines) for following conversions: $NO(g) + H_2(g) \rightarrow 0.5\,N_2(g) + H_2O(g)$ (—), $NO(g) + 0.5H_2(g) \rightarrow 0.5\,N_2O(g) + 0.5H_2O(g)$ (—) and $N_2O(g) + H_2(g) \rightarrow N_2(g) + H_2O(g)$ (—).

the overall reaction $2\,NO(g) + 3H_2(g) + 0.5\,O_2(g) \rightarrow N_2(g) + 3H_2O(g)$ (gas phase: $\Delta_R G(150\,^\circ C) = -838.1\,kJ\,mol^{-1}$, surface reaction: $\Delta_R G(150\,^\circ C) = -796.7\,kJ\,mol^{-1}$). This conversion is described as linear combination of above-mentioned elementary reactions.

$$\Delta_R H_s = E_1 - E_2(0) + E_5 - E_6 + E_7 - E_8 + E_{11} - E_{12} + E_{13} - E_{14} + E_{15} - E_{16}(0) + 0.5(E_{23} - E_{24}) \quad (49)$$

$$\Delta_R S_s = R \ln\left(\frac{A_1}{A_2}\frac{A_5}{A_6}\frac{A_7}{A_8}\frac{A_{11}}{A_{12}}\frac{A_{13}}{A_{14}}\frac{A_{15}}{A_{16}}\left(\frac{A_{23}}{A_{24}}\right)0.5\right) \quad (50)$$

$$\Delta_R H_s = 0.5(E_1 - E_2(0) + E_5 - E_6 + E_7 - E_8 + E_{11} - E_{12}) + E_{13} - E_{14} + 0.5(E_{15} - E_{16}(0) + E_{19} - E_{20} + E_{22} - E_{21}) \quad (51)$$

$$\Delta_R H_s = R\ln\left(\left(\frac{A_1}{A_2}\frac{A_5}{A_6}\frac{A_7}{A_8}\frac{A_{11}}{A_{12}}\right)0.5\frac{A_{13}}{A_{14}}\left(\frac{A_{15}}{A_{16}}\frac{A_{19}}{A_{20}}\frac{A_{22}}{A_{21}}\right)0.5\right) \quad (52)$$

$$\Delta_R H_s = E_1 - E_2(0) + E_5 - E_6 + E_7 - E_8 + E_{11} - E_{12} + E_{15} - E_{16}(0) - E_{19} + E_{20} + E_{21} - E_{22} + E_{23} - E_{24} \quad (53)$$

$$\Delta_R S_s = R\ln\left(\frac{A_1}{A_2}\frac{A_5}{A_6}\frac{A_7}{A_8}\frac{A_{11}}{A_{12}}\frac{A_{15}}{A_{16}}\frac{A_{20}}{A_{19}}\frac{A_{21}}{A_{22}}\frac{A_{23}}{A_{24}}\right) \quad (54)$$

4. Conclusions

It was recently shown that $Pt/WO_3/ZrO_2$ exhibits high low-temperature activity and pronounced N_2 selectivity in the NO_x reduction by H_2 under O_2-rich conditions. For the advancement of the understanding of this reaction, we developed an elementary kinetic mean field model based on a systematic series of kinetic studies and a reaction mechanism suggested in the literature. The model included 6 gas-phase and 8 surface species forming a network of 48 forward and backward reactions. To reduce the number of free kinetic parameters, the catalytic H_2–O_2 reaction was modelled independently and then the NO_x reduction implying the formation of N_2 and N_2O was implemented. Pre-exponential factors were estimated from kinetic gas theory and some kinetic parameters were adopted from the literature, while remaining parameters were obtained by numeric fitting. The constructed model of the H_2–O_2–NO_x reaction on $Pt/WO_3/ZrO_2$ was useful to predict experiments and was found to reveal appropriate thermodynamic consistency showing the relevance of the kinetic model.

Finally, it should be stated that despite the good thermodynamic correspondence of the kinetic model, some differences of experiments and predictions remain. These deviations are partially referred to the mean field approach, which assumes all Pt sites to be equivalent. However, it should also be taken into consideration that a multitude of kinetic parameters had to be adopted from related Pt catalysts. Therefore, we suppose that the experimental evaluation of more kinetic parameters specific for $Pt/WO_3/ZrO_2$ might complement the model.

Acknowledgments

FJPS and SK thankfully acknowledge the financial support from the German Research Foundation (DFG project KU 1459/3-2). The authors also thank Umicore for coating the honeycomb substrate.

References

[1] M.V. Twigg, Appl. Catal. B: Environ. 70 (2007) 2.

[2] R.M. Heck, R.J. Farrauto, S.T. Gulati, Catalytic Air Pollution Control: Commercial Technology, J. Wiley, New York, 2002.
[3] O. Deutschmann,), in: G. Ertl, H. Knözinger, F. Schüth, J. Weitkamp (Eds.), Handbook of Heterogeneous Catalysis, vol. 6, Wiley-VCH Weinheim, 2008.
[4] H. Hirano, T. Yamada, K.I. Tanaka, J. Siera, B.E. Nieuwenhuys, Stud. Surf. Sci. Catal. (New Front. Catal. A) 75 (1993) 345.
[5] M.Y. Smirnov, D.Y. Zemlyanov, E.I. Vovk, Kinet. Catal. 48 (2007) 853.
[6] D.D. Hibbitts, R. Jiménez, M. Yoshimura, B. Weiss, E. Iglesia, J. Catal. 319 (2014) 95.
[7] L. Olsson, E. Fridell, J. Catal. 210 (2002) 340.
[8] O. Deutschmann, J.-D. Grunwaldt, Chem. Ing. Tech. 85 (2013) 595.
[9] Y. Huang, Y. Cheng, C. Lambert, SAE Tech Paper Ser. 01 (2008) 1021.
[10] P. Balle, B. Geiger, D. Klukowski, M. Pignatelli, S. Wohnrau, M. Menzel, I. Zirkwa, G. Brunklaus, S. Kureti, Appl. Catal. B: Environ. 91 (2009) 587.
[11] D.W. Fickel, E. D'Addio, J.A. Lauterbach, R.F. Lobo, Appl. Catal. B 102 (2011) 441.
[12] S. Brandenberger, O. Kroecher, A. Tissler, R. Althoff, Catal. Rev. Sci. Eng. 50 (2008) 492.
[13] M.P. Ruggeri, T. Selleri, M. Colombo, I. Nova, E. Tronconi, J. Catal. 311 (2014) 266.
[14] N. Fekete, R. Kemmler, D. Voigtländer, B. Krutzsch, E. Room, G. Wenninger, W. Strehlau, J.A.A. van den Tillaart, J. Leyrer, E.S.W. Lox Müller, SAE Paper 960 (2014) 133.
[15] G. Liu, P.-X. Gao, Catal. Sci. Technol. 1 (2011) 552.
[16] I. Nova, L. Lietti, L. Castoldi, E. Tronconi, P. Forzatti, J. Catal. 239 (2006) 244.
[17] T. Szailer, J.H. Kwak, D.H. Kim, J.C. Hanson, C.H.F. Peden, J. Szanyi, J. Catal. 239 (2006) 51.
[18] K. Polychronopouloun, A.M. Efstathiou, Recent Pat. Mater. Sci. 5 (2012) 87.
[19] H. Hamada, M. Haneda, Appl. Catal. A: Gen. 421 (2012) 1.
[20] C.N. Costa, V.N. Stathopoulos, V.C. Belessi, A.M. Efstathiou, J. Catal. 197 (2001) 350.
[21] C.N. Costa, P.G. Savva, C. Andronikou, P.S. Lambrou, K. Polychronopoulou, V.C. Belessi, V.N. Stathopoulos, P.J. Pomonis, A.M. Efstathiou, J. Catal. 209 (2002) 456.
[22] C.N. Costa, A.M. Efstathiou, J. Phys. Chem. C 111 (2007) 3010.
[23] C.N. Costa, P.G. Savva, J.L. Fierro, A.M. Efstathiou, Appl. Catal. B: Environ. 75 (2007) 147.
[24] G.G. Olympiou, A.M. Efstathiou, Chem. Eng. J. 170 (2011) 424.
[25] F.J.P. Schott, P. Balle, J. Adler, S. Kureti, Appl. Catal. B: Environ. 87 (2009) 18.
[26] M. Leicht, F.J.P. Schott, S. Kureti, Appl. Catal. B: Environ. 117 (2012) 275.
[27] G.L. Chiarello, D. Ferri, J.-D. Grunwaldt, L. Forni, A. Baiker, J. Catal. 252 (2007) 137.
[28] J.P. Breen, R. Burch, C. Hardacre, C.J. Hill, C. Rioche, J. Catal. 246 (2007) 1.
[29] S. Tamm, N. Vallim, M. Skoglundh, L. Olsson, J. Catal. 307 (2013) 153.
[30] S.P. Kim, M.K. Kim, B.K. Cho, I.-S. Nam, S.H. Oh, J. Catal. 301 (2013) 65.
[31] R. Burch, P.J. Millington, A.P. Walker, Appl. Catal. B: Environ. 4 (1994) 65.
[32] S. Wagloehner, D. Reichert, D. Leon-Sorzano, P. Balle, B. Geiger, S. Kureti, J. Catal. 260 (2008) 305.
[33] J. Siera, P. Cobden, K. Tanaka, B.E. Nieuwenhuys, Catal. Lett. 10 (1991) 335.
[34] O. Deutschmann, R. Schmidt, F. Behrendt, J. Warnatz, Proc. Combust. Inst. 26 (1996) 1747.
[35] D.E. Mears, Ind. Eng. Chem. Process. Des. Dev. 10 (1971) 541.
[36] B. Hellsing, B. Kasemo, S. Ljungström, A. Rosen, T. Wahnström, Surf. Sci. 189 (1987) 851.
[37] J. Warnatz, M.D. Allendorf, R.J. Kee, M.E. Coltrin, Combust. Flame 96 (1994) 393.
[38] O. Deutschmann, F. Behrendt, J. Warnatz, Catal. Today 21 (1994) 461.
[39] T. Finke, M. Gernsbeck, U. Eisele, C. Vincent, M. Hartmann, S. Kureti, H. Bockhorn, Thermochim. Acta 473 (2008) 32.
[40] D.H. Parker, M.E. Bartram, B.E. Koel, Surf. Sci. 217 (1989) 489.
[41] D.K. Zerkle, M.D. Allendorf, M. Wolf, O. Deutschmann, J. Catal. 196 (2000) 18.
[42] L. Olsson, B. Westerberg, H. Persson, E. Fridell, M. Skoglundh, B. Andersson, J. Phys. Chem. B 103 (1999) 10433.
[43] D. Chatterjee, O. Deutschmann, J. Warnatz, Faraday Discuss. 119 (2001) 371.
[44] M. Crocoll, S. Kureti, W. Weisweiler, J. Catal. 229 (2005) 480.
[45] M. Shimizu, Nat. Bur. Stand. (U. S.) Spec. Publ. 323 (1971) 685.
[46] K. Sawabe, Y. Matsumoto, Surf. Sci. 283 (1993) 126.
[47] J. Koop, O. Deutschmann, Appl. Catal. B: Environ. 91 (2009) 47.
[48] A. Burcat, W.C. Gardiner, Combustion Chemistry, Springer, 1984.
[49] C.T. Campbell, G. Ertl, H. Kuipers, J. Segner, Surf. Sci. 107 (1981) 220.
[50] A.B. Mhadeshwar, H. Wang, D.G. Vlachos, J. Phys. Chem. B 107 (12) (2003) 721.
[51] Y.Y. Yeo, L. Vattuone, D.A. King, J. Chem. Phys. 106 (1997) 392.
[52] J. Xu, M.P. Harold, V. Balakotaiah, Appl. Catal. B: Environ. 89 (2009) 73.
[53] M.W. Chase, J. Phys. Chem. Ref. Data 9 (1998) 1.
[54] W.D. Mieher, W. Ho, Surf. Sci. 322 (1995) 151.
[55] J.M. Bradley, A. Hopkinson, D.A. King, J. Phys. Chem. 99 (17) (1995) 032.
[56] J. Xu, R. Clayton, V. Balakotaiah, M.P. Harold, Appl. Catal. B: Environ. 77 (2008) 395.
[57] C.N. Costa, A.M. Efstathiou, Appl. Catal. B: Environ. 72 (2007) 240.
[58] J.M. Garcıía-Cortés, J. Pérez-Ramıírez, J.N. Rouzaud, A.R. Vaccaro, M.J. Illán-Gómez, C. Salinas-Martınez de Lecea, J. Catal. 218 (2003) 111.
[59] D. Vogel, C. Spiel, Y. Suchorski, A. Trinchero, R. Schlögl, H. Grönbeck, G. Rupprechter, Angew. Chem. Int. Ed. (Eng.) 51 (10) (2012) 041.
[60] C.N. Costa, A.M. Efstathiou, J. Phys. Chem. B 108 (2004) 2620.